Yuan *et al. Microstructures* **2025**, *5*, 2025032
DOI: 10.20517/microstructures.2024.82

Microstructures

Research Article

Open Access

Precipitation-assisted heterostructure in a FeMnCoCrCuC high entropy alloy enables superior mechanical property

Ye Yuan[1], Jie Min[1], Haizheng Pan[1], Jiajun Wang[1], Yuliang Yang[1], Mingwei Zhu[2], Weiye Chen[3], Nan Jia[1]

[1]Key Laboratory for Anisotropy and Texture of Materials (Ministry of Education), School of Materials Science and Engineering, Northeastern University, Shenyang 110819, Liaoning, China.
[2]School of Materials Science and Engineering, Shenyang Aerospace University, Shenyang 110136, Liaoning, China.
[3]School of Materials Science and Engineering, North Minzu University, Yinchuan 750021, Ningxia, China.

Correspondence to: Prof. Nan Jia, Key Laboratory for Anisotropy and Texture of Materials (Ministry of Education), School of Materials Science and Engineering, Northeastern University, No. 3-11 Wenhua Road, Heping District, Shenyang 110819, Liaoning, China. E-mail: jian@atm.neu.edu.cn; Prof. Mingwei Zhu, School of Materials Science and Engineering, Shenyang Aerospace University, No.37 Daoyi South Avenue, Shenbei New Area, Shenyang 110136, Liaoning, China. E-mail: mwzhu@sau.edu.cn

How to cite this article: Yuan, Y.; Min, J.; Pan, H.; Wang, J.; Yang, Y.; Zhu, M.; Chen, W.; Jia, N. Precipitation-assisted heterostructure in a FeMnCoCrCuC high entropy alloy enables superior mechanical property. *Microstructures* **2025**, *5*, 2025032. https://dx.doi.org/10.20517/microstructures.2024.82

Received: 2 Sep2024 **First Decision:** 19 Oct 2024 **Revised:** 7 Nov 2024 **Accepted:** 19 Nov 2024 **Published:** 20 Mar 2025

Academic Editor: Huijun Li **Copy Editor:** Ping Zhang **Production Editor:** Ping Zhang

Abstract

High-entropy alloys in which the face-centered cubic structure is dominant cannot meet practical engineering application requirements due to their insufficient strength. Traditional strengthening methods can improve strength of materials, but they inevitably lead to decreased ductility. In this work, mechanical properties of a face-centered cubic-structured FeMnCoCrCu high-entropy alloy were improved by doping a substantial amount of carbon and employing a processing route that combines cold rolling and annealing. A dual-heterostructure characterized by both bimodal grain-size distribution and non-uniform distribution of nanoscale precipitates was constructed. The average grain sizes were 21.6 and 5.9 μm for the coarse and fine grains, accounting for 56.6% and 43.4% of the material, respectively. On the other hand, the finer $M_{23}C_6$ precipitates in the grain interior had an average size of 73.1 nm, constituting 3.4% of the coarse-grained region and 10.7% of the fine-grained region. The larger $M_{23}C_6$ precipitates at grain boundaries had an average size of 182.4 nm, with an overall volume fraction of 1.5%. This heterogeneous microstructure endowed the alloy with superior strength and work-hardening capacity compared to the carbon-free alloy. The yield and tensile strengths reached 500 MPa and 979 MPa, respectively, while maintaining a uniform elongation of 42%. This study not only identifies the origin of strengthening and micromechanism of plastic deformation in the carbon-alloyed dual-heterostructured alloy but also elucidates the formation of the specified microstructure. The findings provide theoretical guidance for developing advanced alloys with both high strength and good ductility.

Keywords: High-entropy alloy, carbon doping, heterostructure, precipitate, mechanical property

INTRODUCTION

High-entropy alloys (HEAs), also known as multi-principal elemental alloys (MPEAs), have attracted widespread attention in the field of materials science owing to their unique design concept and numerous excellent properties[1-5]. In recent years, the development of advanced metallic materials that meet the demands of high strength, high ductility and environmental sustainability has become a hot topic[6-9]. Among those, Li *et al.* designed the $Fe_{50}Mn_{30}Co_{10}Cr_{10}$ HEA based on the equimolar CoCrFeMnNi alloy, successfully enhancing both strength and ductility by introducing the transformation-induced plasticity (TRIP) mechanism[5]. However, the FeMn-based HEAs in which the face-centered cubic (fcc) structure is dominant usually exhibit low yield strength, rendering them unable to meet the growing demand for advanced structural materials. Consequently, researchers have employed various strengthening methods to enhance strength of the alloys while aiming to maintain good ductility. These methods include doping with interstitial and substitutional solute atoms[3,10-13], introducing nanoscaled precipitates[11-13], increasing defects such as twin boundaries, high-density dislocations and phase interfaces[14,15], and refining grains[13,16].

However, traditional strengthening methods, including solid solution, grain refinement, deformation and precipitation strengthening, often lead to a significant increase in strength but a substantial loss in plasticity. In recent years, the design strategy of “heterostructured (HS)” materials has gained widespread attention, as it has been proven to be an effective method for improving strength for metallic materials without significantly damaging their ductility. HS materials, particularly for structural applications, are composed of hard and soft domains with significant differences in mechanical properties (> 100%). The two domains exhibit a synergistic effect during co-deformation, resulting in overall mechanical properties that are superior to those predicted by the rule of mixture[17,18]. During deformation, the soft domains undergo plastic deformation first, while the hard domains are still in the elastic regime. To ensure the continuity of deformation, geometrically necessary dislocations (GNDs) are generated near the heterogeneous interfaces within the soft domains. The accumulation of GNDs leads to hetero-deformation-induced (HDI) stress, thereby enhancing the strength of materials and delaying plastic instability[19,20]. Currently, various heterostructures have been developed to improve the performance of alloys, including HS lamellar structures[21,22], bimodal and multimodal structures[23-25], gradient structures[26-28], dual-phase structures[5,29], harmonic structures[30], layered structures[31], and heterogeneous composite structures[18]. Among these, the earliest HS material that attracted great attention was the HS lamellar structures in pure Ti, as reported by Wu *et al.*[21]. By combining asymmetric rolling (87.5%) with partial recrystallization annealing (holding at 475 °C for 5 min), the soft domains with a 25% recrystallization fraction were embedded in a lamellar form within the non-recrystallized hard domains. This HS material not only exhibited high yield strength (972 MPa) and 8.9% uniform elongation comparable to the ultrafine-grained Ti, but also demonstrated superior strain hardening capacity compared to the coarse-grained (CG) Ti. Sun *et al.*[28] performed surface mechanical attrition treatment (SMAT) on the 304 stainless steel and successfully produced a bulk sample with the gradient structure. The gradient structure comprised varying proportions of austenite and α’-martensite, grain size, and dislocation density that change with the depth from the material surface. Specifically, the outer layers on both sides of the sample primarily consisted of α’-martensite grains with an average size of 36 nm, while the center of the sample only contained austenitic grains with an average size of 23 μm. This gradient microstructure contributed to an additional strain hardening capacity for the material, ultimately achieving an ultra-high yield strength of 1,073 MPa and a uniform elongation of 21%. Li *et al.*[30]

also successfully prepared non-equiatomic FeMnCoCr HEAs with adjustable shell fractions (16%-70%) in a harmonic structure using mechanical milling (MM) and subsequent spark plasma sintering (SPS). The core region was composed of coarse grains with a grain size of 8 μm, while the shell region consisted of ultrafine grains with a grain size smaller than 1 μm. Compared to homogeneous microstructure, these harmonically structured samples exhibited simultaneous enhancement of strength and strain hardening capacity. The high strength is mainly attributed to grain refinement and precipitate-induced strengthening, while the higher strain hardening rate is due to HDI hardening and the activation and interaction of various deformation mechanisms within the shell region.

In recent years, researchers have not been satisfied with the strengthening effects brought by one single heterostructure and begun to combine multiple heterostructures within individual materials. For instance, Li *et al.*[32] introduced a coherent $L1_2$ phase rich in Ni, Al, and Ti into a non-equimolar NiCoCr medium-entropy alloy (MEA). By combining rolling with the subsequent annealing, dual heterostructures characterized by bimodal grain sizes and a non-uniform distribution of precipitates were obtained. Specifically, the proportions and average grain sizes of the CG and fine-grained (FG) regions were 67.4%/4.7 μm and 32.6%/15.0 μm, respectively. The proportions and average sizes of the submicron- and nanoscale precipitates were 18.7%/184.8 nm and 11.7%/16.5 nm, respectively. This alloy exhibited a yield strength of 1,200 MPa, a tensile strength of 1,560 MPa, and a total elongation of 33.6%. The ultra-high strength mainly resulted from the HDI strengthening effect. The activation of high-density stacking faults (SFs) and Lomer-Cottrell (L-C) locks within the dual heterostructure, as well as the low lattice mismatch between the $L1_2$ phase and the matrix, reduced stress concentration and delayed plastic instability, thereby leading to excellent work hardening capability. Similarly, Guo *et al.*[33] introduced various strengthening phases, including the coherent nanoscale D022-γ' precipitate phase, by doping V and Ta into a NiCoCr alloy, and combined it with aging treatment. These heterostructures also resulted in a good balance of strength and ductility.

Inspired by previous studies, we focus on a fcc-structured $Fe_{50}Mn_{27}Co_{10}Cr_{10}Cu_3$ HEA. By doping with C element (x = 0, 0.5, 1, 2, 3 at.%) and applying a process combining cold rolling (60%) and annealing at 1,000 °C, we enhance the mechanical properties of the alloy. When the C content reached 3 at.%, a material with dual-heterostructure characteristics, namely bimodal grain sizes and non-uniformly distributed precipitates, is obtained. Compared to the homogeneous grain structure of the carbon-free alloy, the dual heterostructures in the carbon-doped alloy provide higher strength and work-hardening capacity while maintaining good ductility. We also systematically analyze the formation and evolution of the dual heterostructure, and the strengthening and deformation mechanisms of the alloy. These findings are expected to provide theoretical guidance for designing alloys with a good combination of high strength and ideal ductility.

EXPERIMENTAL PROCEDURE

Material preparation

In this work, $Fe_{50}Mn_{27-x}Co_{10}Cr_{10}Cu_3C_x$ HEAs with x ranging from 0 to 3 at.% were studied. The $Fe_{50}Mn_{27}Co_{10}Cr_{10}Cu_3$ alloy was derived from the $Fe_{50}Mn_{30}Co_{10}Cr_{10}$ HEA by replacing an equivalent amount of Mn with 3 at.% Cu. This modification aims to increase the SF energy (SFE) of the alloy system, resulting in the absence of martensite both before and after deformation, which will be shown in the X-ray diffraction (XRD) and transmission electron microscope (TEM) analysis. Initially, high-purity metals (> 99.95 wt.%) were selected as raw materials, and alloys were melted in a vacuum arc melting furnace under an argon protective atmosphere. The melting process was repeated at least five times with continuous electromagnetic stirring. The as-cast alloys were subjected to a solution treatment at 1,200 °C for 4 h followed by air cooling to ensure uniform composition and microstructure. It should be noted that the alloys were not hot rolled, but were directly cold-rolled to avoid cracking of the copper-containing alloys during hot deformation[34,35]. Subsequently, the alloys were cut into plates with dimensions of 40 mm in length, 25 mm in width, and 4.5 mm in thickness using an electrical discharge wire-cutting machine. These plates were then cold rolled at room temperature with five passes to reach a total reduction of 40%. The cold-rolled plates were encapsulated in vacuum quartz tubes, followed by annealing at 1,200 °C for two hours and air cooling. Afterward, the alloys underwent multiple passes of cold rolling at room temperature with a total reduction of 60%. Finally, these cold-rolled plates were annealed in a salt bath at 1,000 °C for three minutes. The detailed process of sample preparation is illustrated in Figure 1. In the following text, the alloys obtained through the above thermo-mechanical processing route are sequentially named C0, C0.5, C1, C2, and C3 alloys, according to their different C contents (0-3 at.%).

Microstructure characterization

The phase composition of the alloy was characterized using a Smartlab XRD instrument equipped with CuK α1 radiation (λ = 0.154056 nm). The scanning range was 40-100°, with a scanning rate of 5°/min. Microstructures before and after tensile deformation were characterized using a JSM-7001F scanning electron microscope (SEM), a ZEISS Crossbeam 550 SEM equipped with an electron backscatter diffraction (EBSD) probe, and a JEM 2100F TEM. Compositions of the matrix and precipitates were also analyzed using high-precision Gemini SEM 560 equipment. For SEM and EBSD analysis, samples were initially mechanically polished with sandpaper to remove surface oxides. Subsequently, electrolytic polishing was performed using a mixed solution of $HClO_4$: C_2H_5OH=1:15 (vol.%) at a polishing voltage of 20 V for 20 s, maintaining the solution temperature at -20 °C. EBSD mapping was conducted with a step size of 80 nm, and the obtained data were processed and analyzed using the Channel 5 software. TEM samples were first mechanically polished to a thickness of 50 μm. They were then thinned using a TenuPol-5 twin-jet electropolisher at -25 °C and 25 V, using an electrolyte solution of $HClO_4$:C_2H_5OH=1:10 (vol.%). The sample coordinate system was defined by three orthogonal directions, i.e., rolling direction (RD), transverse direction (TD), and normal direction (ND). SEM and EBSD samples were taken from the longitudinal section (RD-ND plane) of the rolled plate, while TEM samples were taken from the rolling surface (RD-TD plane). The size and volume fraction of grains and precipitates for each material were statistically obtained from microstructure images using Image J software. To ensure the accuracy of the experimental results, these data were based on the average values obtained by characterizing five or more different regions.

Mechanical property testing

Uniaxial tensile tests and loading-unloading-reloading (LUR) cyclic tensile tests were conducted using an AG-XPLUS 100 kN universal testing machine at room temperature. The tests were performed along the RD of the plate with a strain rate of 1×10^{-3} s^{-1}. It should be noted that both the rolled and annealed samples exhibit weak texture components (see Supplementary Figures 1 and 2). Accordingly, mechanical properties in the RD and TD directions show insignificant changes (see Supplementary Figure 3), indicating isotropic mechanical properties of the alloys. The more detailed information can be found in the Supplementary Note "Texture Analysis". In the LUR tests, the specimens were first stretched to 1% engineering strain, and then unloaded to 30 MPa. Subsequently, the LUR process was repeated at every 4% engineering strain interval until the sample fractured. An extensometer was used to accurately measure and control the displacement during testing. The gauge length of the specimens was $24 \times 3 \times 1$ mm^3. To ensure the repeatability of the results, both tensile and LUR tests were conducted three times. Microhardness test was performed with a load of 50 g and a dwell time of 10 s. The hardness measurements were taken at 20 different locations for each sample, and the average value was reported.

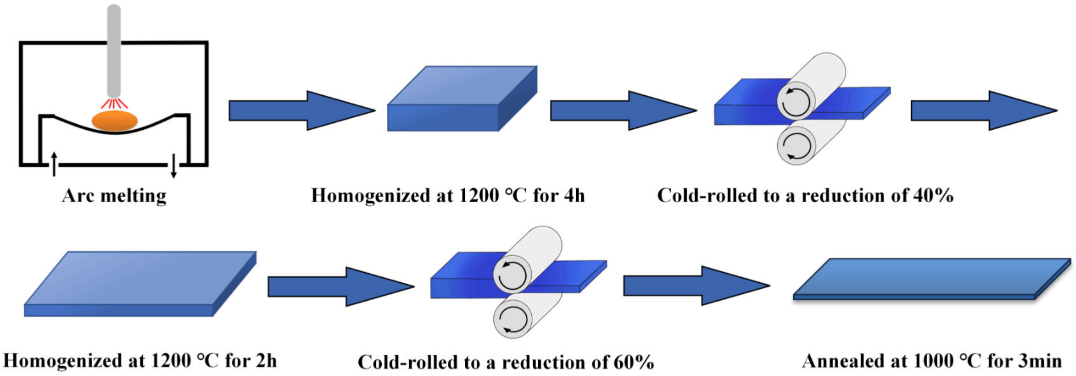

Figure 1. Schematic illustration of the preparation route.

EXPERIMENTAL DATA

Tensile properties

Figure 2A depicts the room-temperature tensile stress-strain curves of the C0, C0.5, C1, C2, and C3 alloys. As the C content increases, yield strength of the alloys gradually grows, while uniform elongation only decreases slightly. Specifically, yield strength (σ_s) and tensile strength (σ_b) of C0 alloy are 223 MPa and 535 MPa, respectively, with a uniform elongation of 57.1%. The C0.5 and C1 alloys show slight improvements in yield and tensile strengths, with yield strengths of 240 MPa and 265 MPa, tensile strengths of 566 MPa and 626 MPa, respectively. Both alloys maintain relatively high uniform elongations of 47.6% and 49.7%. In contrast, the C2 and C3 alloys exhibit a significant increase in yield and tensile strength. The yield strengths for the C2 and C3 alloys are 417 MPa and 500 MPa, with tensile strengths of 856 MPa and 979 MPa, respectively. The uniform elongations decrease slightly to 38.1% and 42.0%, respectively (detailed tensile properties are summarized in Supplementary Table 1). The corresponding tensile true stress-true strain curves and strain hardening rate curves are shown in Figure 2B and C. The strain hardening rate curves of the alloys consist of three stages. Taking the C3 alloy as an example, firstly, the strain hardening rate rapidly decreases with increasing true strain (Stage I, true strain < 0.03). Then, the rate of decrease slows down (Stage II, true strain is between 0.03 and 0.34). Finally, as deformation continues, the strain hardening rate rapidly decreases until the sample fractures (Stage III, true strain > 0.34). Notably, the strain hardening capability monotonically increases with the C content. Specifically, at a true strain of 0.2, the strain hardening rate for the C0 alloy is 1,351 MPa. This rate increases to 1,441 MPa and 1,560 MPa for the C0.5 and C1 alloys, respectively. Interestingly, starting from the C2 alloy, the work hardening rate of the alloy significantly increases, with the work hardening rates of C2 and C3 reaching 2,053 and 2,155 MPa, respectively.

Initial microstructure

As mentioned earlier, the C2 and C3 alloys exhibited significantly enhanced mechanical properties compared to the C1 alloy, with notable increase in yield and tensile strengths, slight decrease in uniform elongation, and substantial improvement in work hardening rates. Based on these findings, we selected the carbon-free base alloy C0 as well as the C1 and C3 alloys as the subjects for further investigation. Figure 3 shows the microstructures and corresponding grain size distributions of the C0 and C1 alloys obtained by SEM. Both alloys exhibit completely recrystallized microstructures with similar average grain sizes of 19.9 μm and 18.8 μm, respectively. However, with increased C content, the C3 alloy presents a laminated structure characterized by the alternation of two distinct regions with different contrasts, as shown in Figure 4A. A magnified view of the interface within the red boxed region reveals that this laminated structure consists of CG and FG regions with significantly different grain sizes, both in a completely

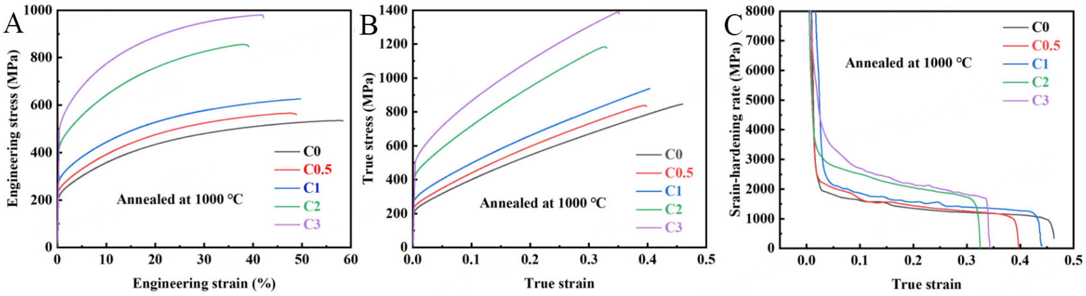

Figure 2. Tensile properties and strain hardening curves of the C0, C0.5, C1, C2 and C3 alloys: (A) engineering stress-strain curves, (B) true stress-strain curves and (C) strain-hardening rate curves.

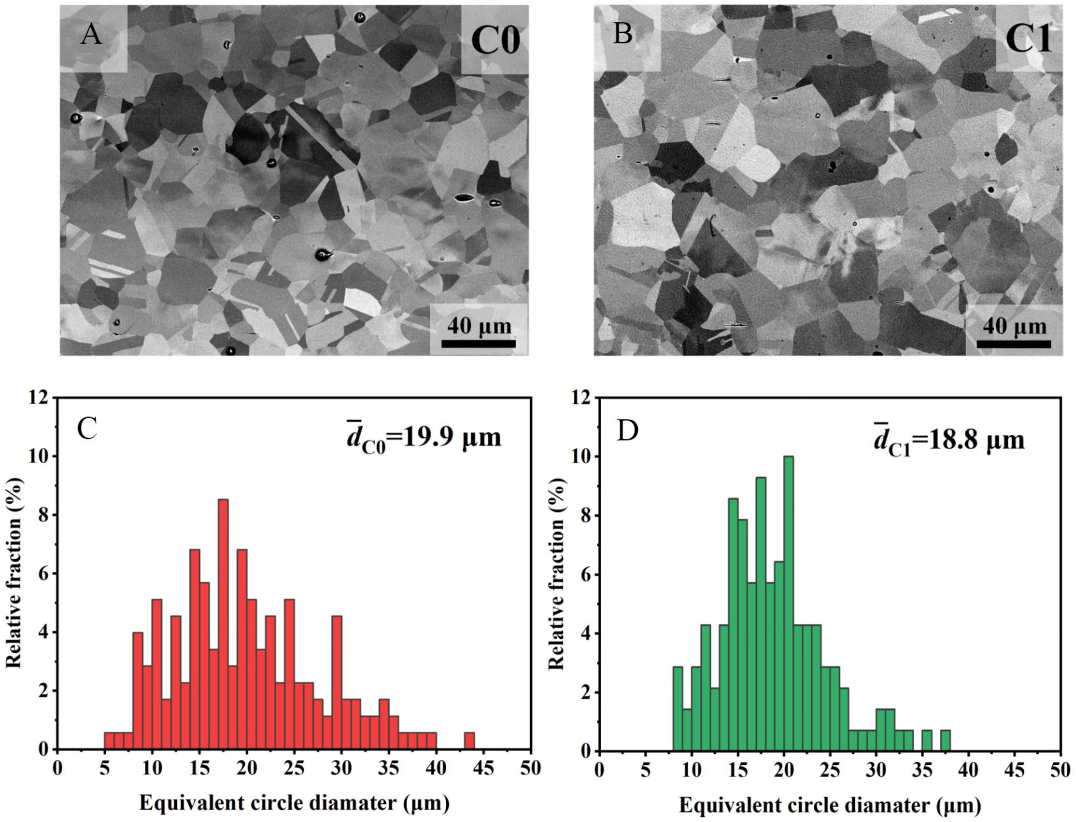

Figure 3. Microstructures of (A) C0 and (B) C1 alloys; (C) and (D) show grain size distributions corresponding to (A) and (B), respectively.

recrystallized state [Figure 4B]. The maximum grain size can reach up to 54.6 μm, while the minimum grain size is only 2.5 μm. By defining coarse and fine grains with a threshold of 10 μm, we conducted a statistical analysis of the grain sizes in these two regions at more than three sample locations. The results indicate that CG regions account for 43.4% of the alloy, while FG regions constitute 56.6%. The average grain sizes are 21.6 μm for the CG regions and 5.9 μm for the FG regions [Figure 4C and D]. Additionally, numerous spherical precipitates are observed at the grain boundaries, with a higher concentration along the grain boundaries of the FG regions compared to the CG regions. A few precipitates are distributed in bands within or across the grains (indicated by yellow arrows in Figure 4). The volume fraction of intergranular precipitates is 1.5%.

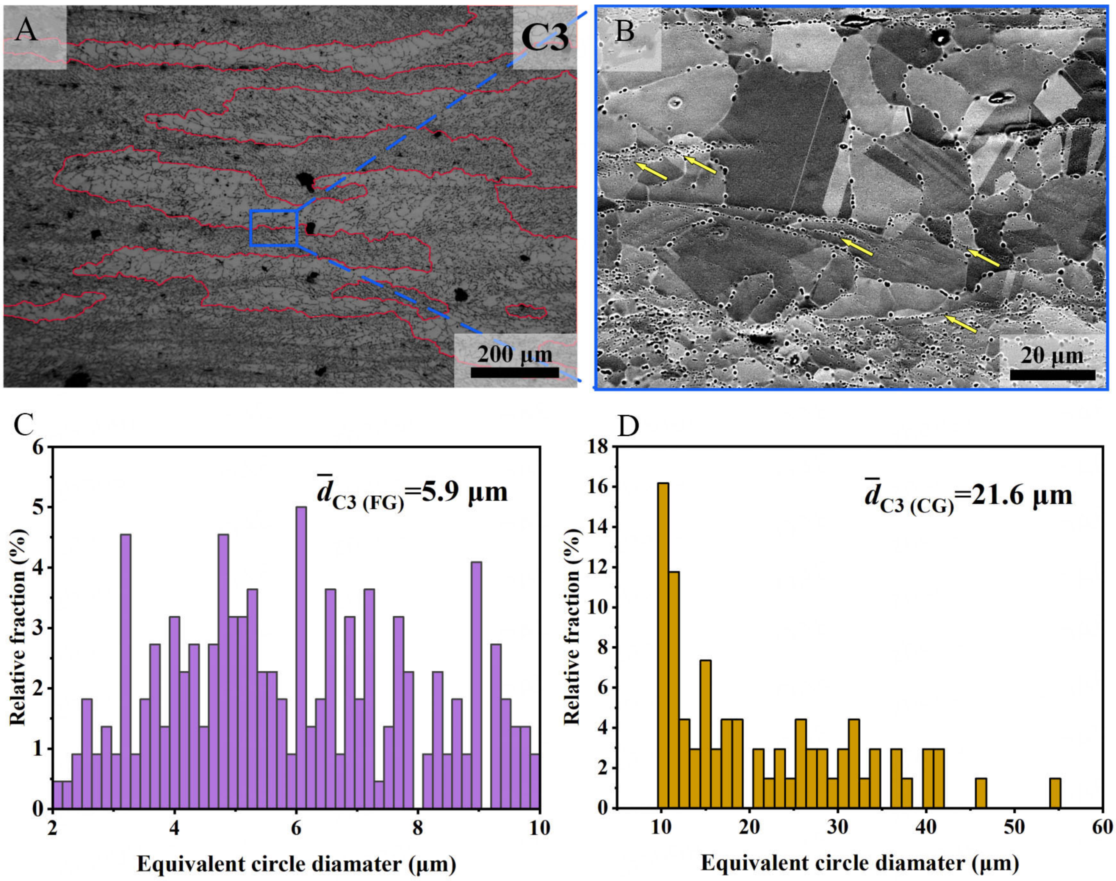

Figure 4. Microstructure of the C3 alloy: (A) macroscopic morphology; (B) enlarged view within the blue box in (A); (C) and (D) grain size distributions within the FG and the CG regions corresponding to (A). The yellow arrows in (B) indicate the band-like distribution of precipitates within or traversing grains. FG: Fine-grained; CG: coarse-grained.

To determine the type and structure of the precipitates, XRD measurements were conducted for the alloys. Unfortunately, only austenite was identified in the XRD pattern, and no precipitates were found [Figure 5A]. This may be due to the small size and low volume fraction of the precipitates (with a minimum size of tens of nanometers; see the text below), which prevents detection of the peaks from $M_{23}C_6$ precipitates. Linear fitting of the relationship between the lattice constant and C content indicates that an increase of 1 at.% C leads to a rise of 0.003 Å in lattice constant [Figure 5B]. Figure 6A shows the morphology of intergranular and intragranular precipitates in the FG regions of the C3 alloy obtained by TEM. Statistical analysis of precipitate sizes at multiple locations (including Figure 7) indicates that intragranular precipitates are smaller, with an average size of 73.1 nm [Figure 6B]. In contrast, intergranular precipitates are relatively large, with an average size of 182.4 nm [Figure 6C]. Selected area electron diffraction (SAED) patterns along the $[0\bar{1}1]$, $[1\bar{2}3]$, [111] and [112] zone axes confirm that the intergranular precipitates at location "1" are $M_{23}C_6$ [Figure 6D1-D4]. Similarly, SAED patterns along the [010], $[1\bar{5}0]$, $[\bar{1}30]$ and $[\bar{1}32]$ zone axes identify that the intragranular precipitates at location "2" are also $M_{23}C_6$ [Figure 6E1-E4]. To further determine the composition of the precipitates, scanning TEM (STEM) combined with energy dispersive X-ray spectroscopy (EDS) was employed, as shown in Figure 7. Analysis of the CG regions reveals that the precipitates mainly exhibit a band distribution, accounting for only 3.4% in CG regions [Figure 7A]. The elemental mapping results indicate that these precipitates are rich in Cr and C, while the contents of Fe, Mn, Co, and Cu are relatively low. In the FG regions, the precipitates are uniformly distributed within grains, with a volume fraction of 10.7% in FG regions. Some large precipitates (with a

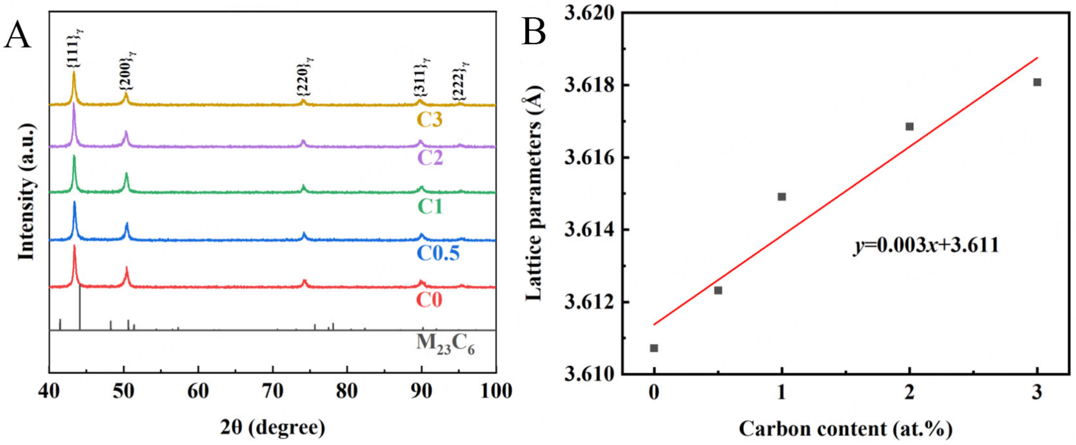

Figure 5. XRD patterns of the $Fe_{50}Mn_{27-x}Co_{10}Cr_{10}Cu_3C_x$ alloys and the evolution of lattice parameter with increasing carbon content. XRD: X-ray diffraction.

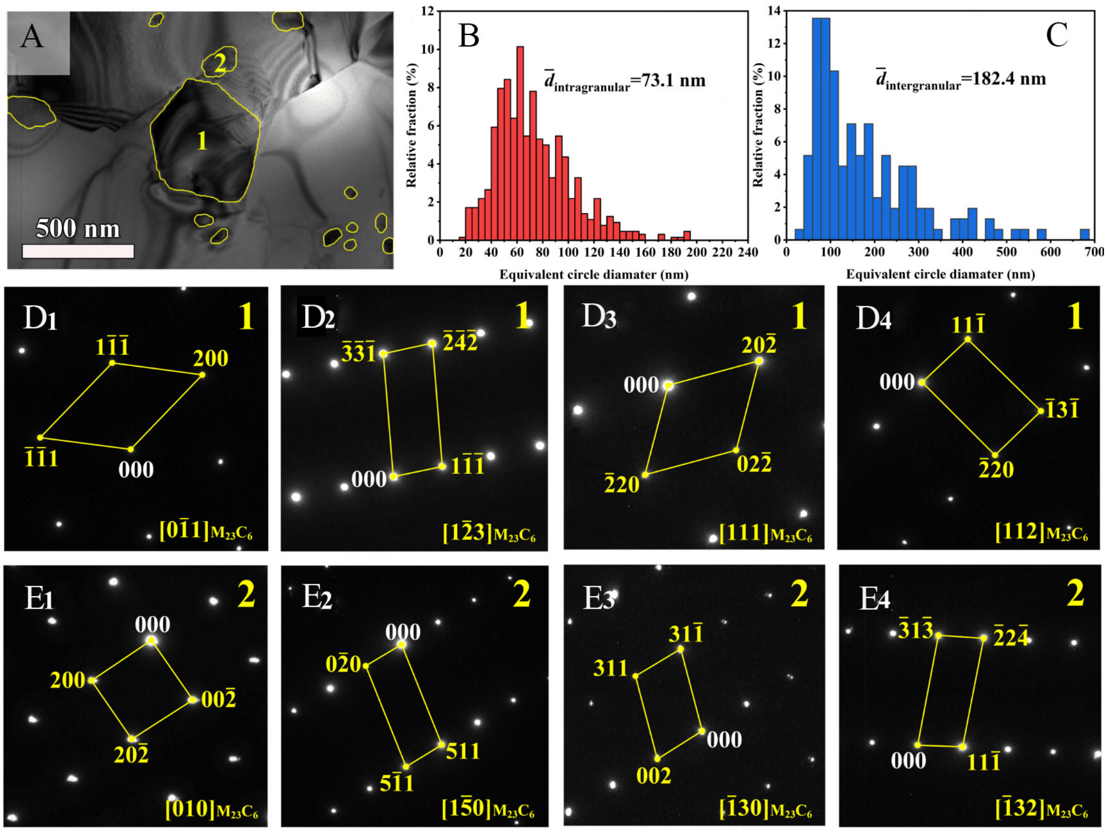

Figure 6. Microstructure of intragranular and intergranular $M_{23}C_6$ precipitates in the C3 Alloy: (A) typical TEM image of $M_{23}C_6$ precipitates; (B and C) precipitate size distribution of intragranular and intergranular precipitates; (D_1-D_4) the SAED patterns of the intergranular precipitates taken from the $[0\bar{1}1]$, $[1\bar{2}3]$, [111] and [112] zone axes, (E_1-E_4) the SAED patterns of the intergranular precipitates taken from the [010], $[1\bar{5}0]$, $[\bar{1}30]$ and [132] zone axes.

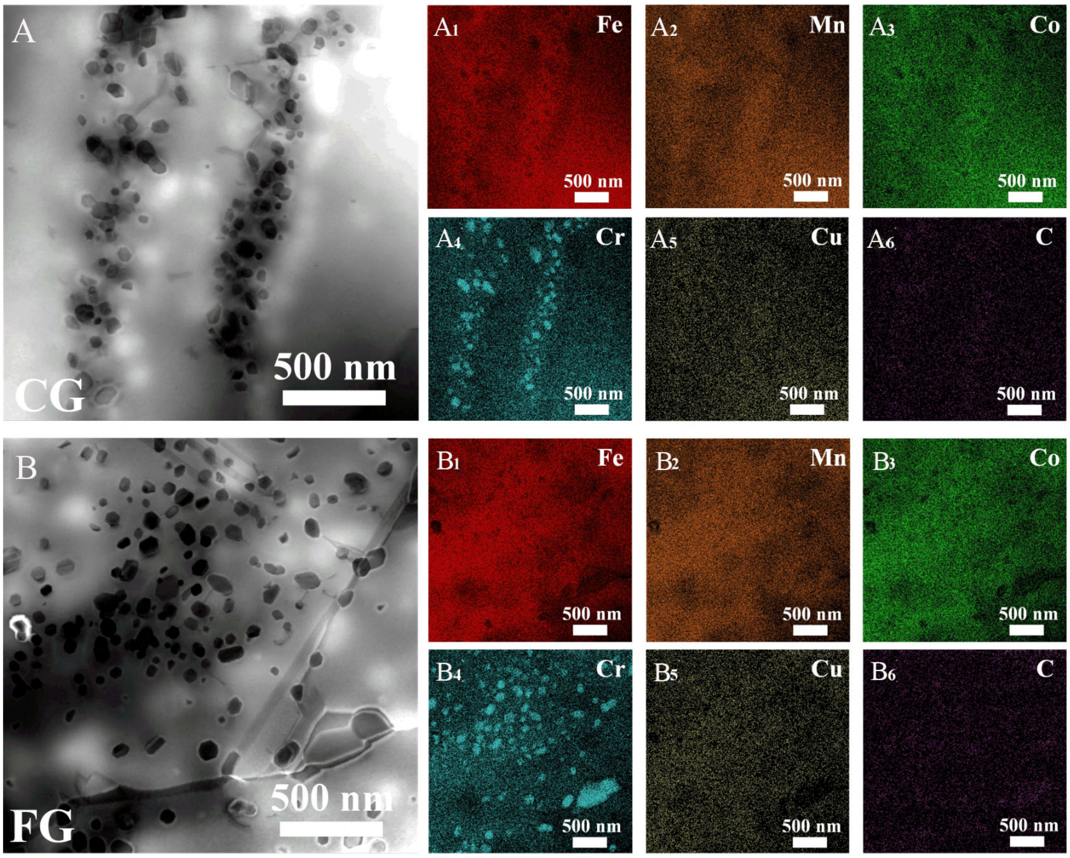

Figure 7. Microstructure and elemental distribution of $M_{23}C_6$ precipitates in the C3 Alloy: (A) STEM image showing the band-like distribution of $M_{23}C_6$ precipitates in the CG region; (B) STEM image displaying $M_{23}C_6$ precipitates in the FG region, (A_1-A_6) and (B_1-B_6) the corresponding EDS mapping of Fe, Mn, Co, Cr, Cu and C elements. STEM: Scanning transmission electron microscope; CG: coarse-grained; FG: fine-grained; EDS: energy dispersive X-ray spectroscopy.

diameter of ~94 nm) are also present at grain boundaries, presenting a similar chemical composition to those in the CG regions. Namely, the precipitates found in both CG and FG regions, as well as within and between grains, are intermetallic compounds rich in Cr and C. Another set of results obtained by using high-precision SEM for the region with triple junctions are presented in Supplementary Figure 4, with the compositions of the precipitates and matrix listed in Supplementary Table 2. The elemental segregation deduced here is consistent with that obtained by TEM. In summary, the C3 alloy exhibits a dual-heterostructure. This structure comprises CG and FG regions with significant differences in grain size, as well as non-uniformly distributed precipitates ranging from tens to over a hundred nanometers.

Microhardness

Vickers hardness measurements at different positions for each alloy are shown in Figure 8. The average hardness of the C0 alloy is 1.6 GPa. Due to the solid solution strengthening effect of C, the average hardness of the C1 alloy increases to 1.9 GPa. Additionally, because the grain size distribution in these two alloys is uniform, the hardness values fluctuate very little across different positions. In contrast, the average hardness in the CG regions of the C3 alloy reaches 2.5 GPa, while the FG regions exhibit a higher average hardness of 3.2 GPa. The difference in hardness between the CG and FG regions is not only attributed to grain size but also to the non-uniform distribution of precipitates. Furthermore, due to the highly inhomogeneous microstructure in this alloy, the hardness values in both CG and FG regions exhibit significant fluctuations.

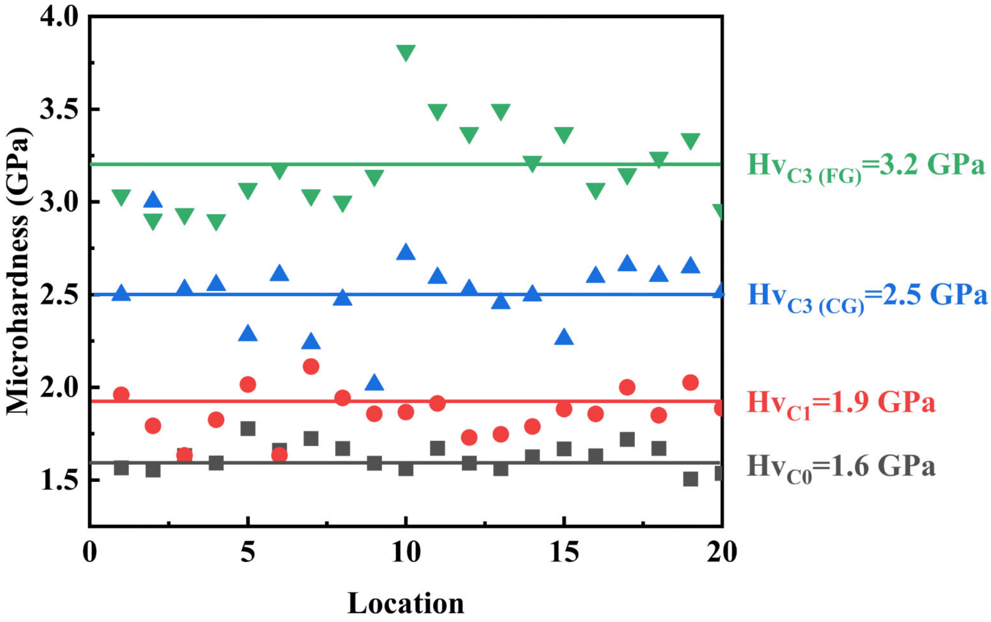

Figure 8. Microhardness measurements for 20 randomly selected locations in C0 and C1 alloys, as well as FG and CG regions of the C3 alloy. FG: Fine-grained; CG: coarse-grained.

Microstructure after tensile deformation

To reveal the mechanisms underlying the significant enhancements in strength and work hardening rate of the C3 alloy compared to the C0 and C1 alloys, we first performed EBSD characterization on the three alloys with a tensile strain of 42% (fracture strain of C3 alloy, corresponding to 0.35 true strain). Figure 9A-C shows the orientation distribution maps, indicating that the grains in all three alloys are elongated along the tensile direction. The corresponding strain distribution is expressed by the Kernel average misorientation (KAM) maps, as shown in Figure 9D-F. Due to the relatively uniform grain distributions in the C0 and C1 alloys, high KAM values are identified only at large-angle grain boundaries [Figure 9D and E]. In contrast, the C3 alloy, with its heterogeneous intergranular and intragranular structure, exhibits generally higher KAM values within the microstructure [Figure 9F]. Detailed KAM value distributions are presented in Figure 9G-I. The C0 and C1 alloys exhibit relatively low average KAM values of 0.95° and 0.86°, respectively. In contrast, the C3 alloy demonstrates a significantly higher average KAM value of 1.79°.

Subsequently, we perform TEM analysis on the three alloys with a tensile strain of 42%, as shown in Figure 10. After tensile deformation, fine intersecting twins are observed in the C0 alloy with an average thickness of 19 nm and an average spacing of 29 nm [Figure 10A]. The corresponding SAED pattern is shown in Figure 10A1. The C0 alloy also contains a significant amount of dislocation cell structures [Figure 10B], which are observed near the [110] zone axis under g = (002) condition [Figure 10B1]. The deformation microstructure of the C1 alloy closely resembles that of the C0 alloy [Figure 10C and D], with the deformed twins having average thickness and spacing of 16 nm and 39 nm, respectively, along with high-density dislocation cell structures. For the C3 alloy, twinning activation is also observed, with the deformed twins exhibiting average width and spacing of 12 nm and 44 nm, respectively [Figure 10E and E1]. High-density dislocation cell structures are similarly present [Figure 10F and F1]. Additionally, extensive dislocation-precipitate interactions are identified within the C3 alloy. Representative uniform and band-like distributions of precipitates are depicted in Figure 10G and H, respectively, with the corresponding dislocation g vectors shown in Figure 10G1 and H1. Regardless of the precipitate distribution

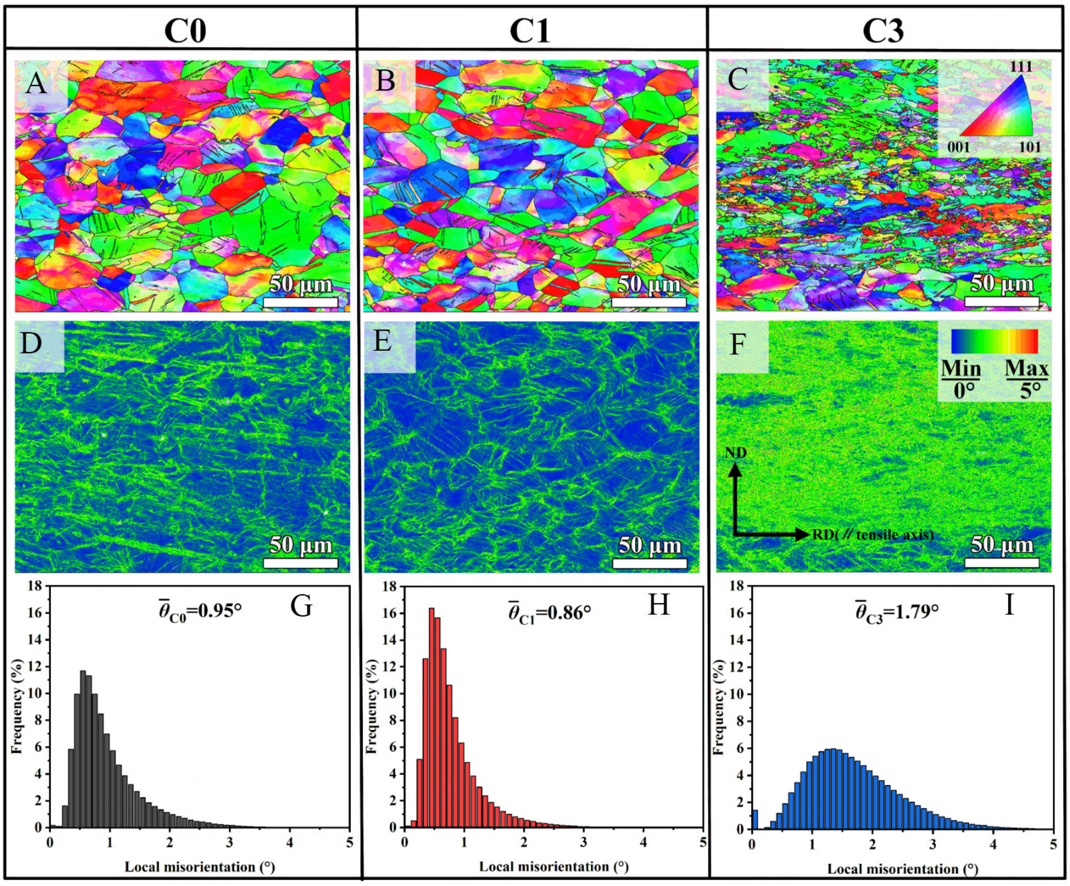

Figure 9. EBSD maps of C0, C1, and C3 alloys after 42% tensile strain: (A-C) orientation distribution maps; (D-F) KAM maps and (G-I) misorientation distribution maps. High-angle grain boundaries, defined as those with misorientation angles above 10°, are indicated by thin black solid lines in (A-C). EBSD: Electron backscatter diffraction; KAM: kernel average misorientation.

type, a significant amount of dislocation entanglement is observed around the precipitates, indicating strong dislocation hindrance effects by the precipitates. The precipitates maintain a prominent spherical morphology, suggesting that they are not sheared by dislocations.

DISCUSSION

Construction of the dual-heterostructure

The dual-heterostructure in the C3 alloy, characterized by bimodal grain sizes and the non-uniform distribution of precipitates, contributes to high strength and excellent work hardening capacity [Figure 2]. It is crucial to have a deep understanding of the formation mechanism of these non-uniform structures, in which the $M_{23}C_6$ precipitates play a key role. We then first analyze the formation of precipitates in the C3 alloy. Microstructural observations of the C3 alloy after solid solution treatment reveal that grain diameter reaches several hundred micrometers [Supplementary Figure 5A]. Further TEM characterization confirms that even with an addition of 3 at.% Cu, no Cu precipitation or other intermetallic compounds formed in the alloy [Supplementary Figure 5B and C]. This indicates that $M_{23}C_6$ precipitates only form during the subsequent short-term annealing process. Subsequently, SEM observations are conducted on the samples annealed at 1,000 °C for 1 min and 2 min. The sample annealed for 1 min has already formed CG and FG regions inside. At this stage, the average grain size of the CG region was smaller (~13.8 μm) compared to the sample annealed for 3 min, but the difference in distribution of $M_{23}C_6$ precipitates has already appeared [Figure 11A]. Specifically, the FG regions contain numerous fine precipitates within the grains, whereas the

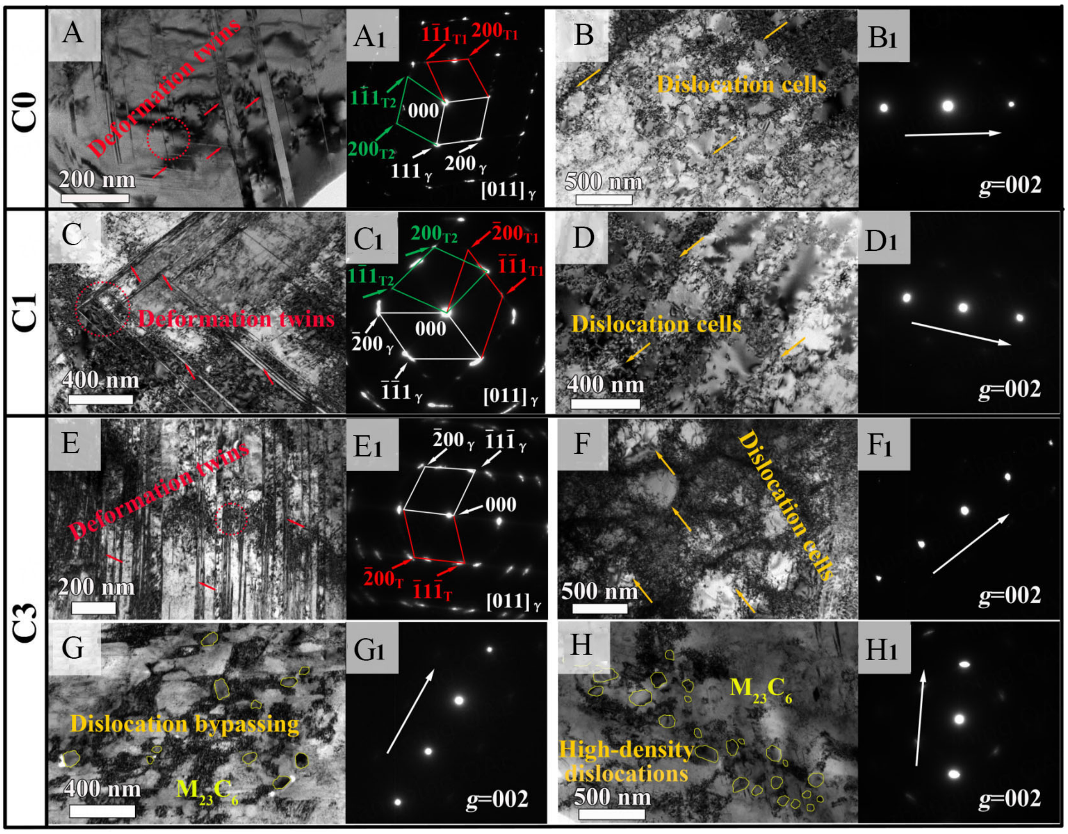

Figure 10. TEM images of the C0, C1 and C3 alloys after 42% tensile deformation: (A-A_1), (C-C_1) and (E-E_1) deformation twins observed in C0, C1 and C3 alloys and the corresponding SAED patterns; (B-B_1), (D-D_1) and (F-F_1) dislocations within the alloys and the corresponding SAED patterns; (G-G_1) interaction between the uniformly distributed $M_{23}C_6$ precipitates and dislocations; (H-H_1) interaction between the $M_{23}C_6$ precipitates within a band-like region and dislocations. Dislocations are observed near the [110] zone axis with g = (002). TEM: Transmission electron microscop; SAED: selected area electron diffraction.

CG regions have a lower density of precipitates. Additionally, precipitates with a size of ~90 nm are present at the grain boundaries [Figure 11B]. As the annealing time extends to 2 min, grains in the CG regions significantly grow, while the grain size in the FG regions remains almost unchanged [Figure 11C]. At this point, the precipitates inside the FG regions slightly increase in size, while their density decreases [Figure 11D]. This suggests that the precipitates exert a strong pinning effect on the grain boundaries.

The formation of the dual-heterostructure in the C3 alloy can be illustrated by a schematic diagram, as depicted in Figure 12. The homogenized alloy exhibits a uniform, equiaxed CG structure. During the subsequent room-temperature rolling process, the degree of deformation of individual grains varies due to their different initial orientations. The regions with a high degree of deformation can provide numerous sites and sufficient energy for the nucleation of new grains and precipitates. Conversely, the regions with less deformation have the lower energy stored, resulting in fewer nucleation sites for precipitates and recrystallization. During deformation, a high density of dislocations and deformation twins is formed. In the following annealing process, in that area with the higher deformation energy, a high density of precipitates and a greater number of recrystallized grains are developed. Twins can serve as fast diffusion pathways for C atoms, allowing some $M_{23}C_6$ precipitates to nucleate along the twin boundaries[36]. As the annealing time increases, the recrystallized grains grow. When the moving grain boundaries encounter $M_{23}C_6$ precipitates, they interact with the precipitates via the well-known Zener pinning effect[37,38]. Then, the

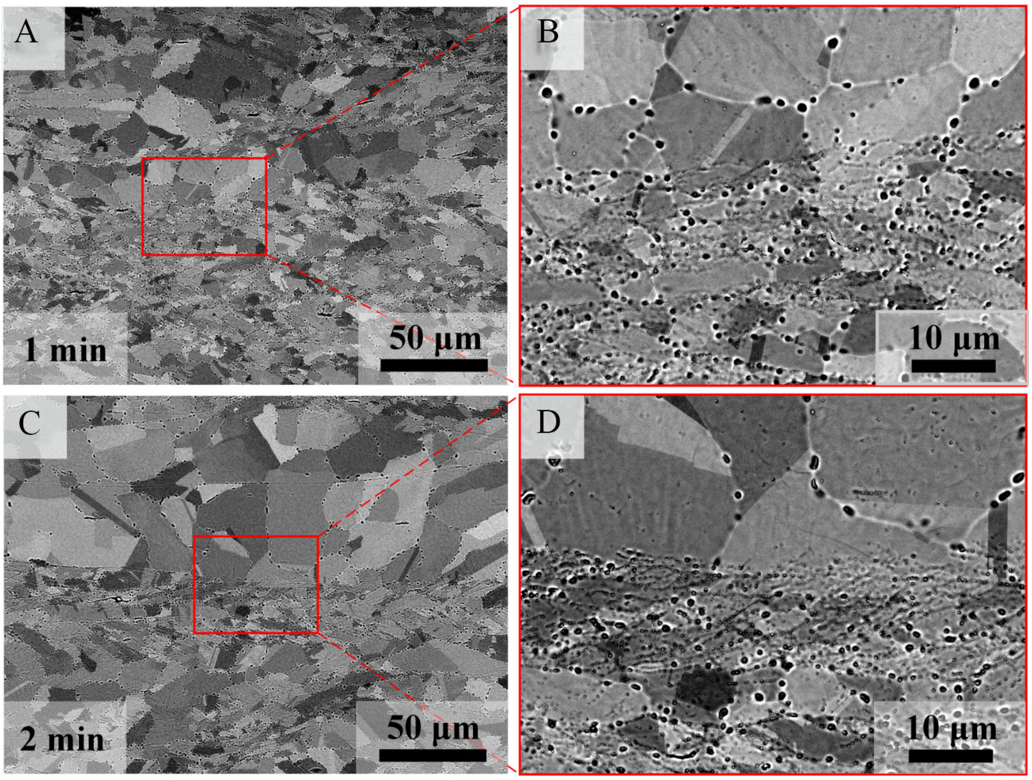

Figure 11. SEM images of the C3 alloy annealed at 1,000 °C for different time durations: (A) 1 min and (C) 2 min; (B) and (D) are the enlarged view of the red dashed rectangles in (A)and (C), respectively. SEM: Scanning electron microscope.

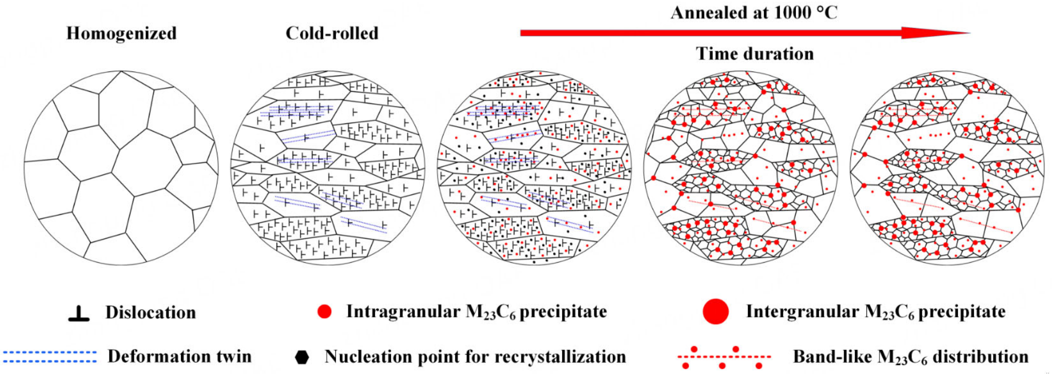

Figure 12. Schematic illustration showing the formation of the dual-heterostructure in the C3 alloy during thermomechanical processing.

high interfacial energy and relatively weak bonding in grain boundaries leads to precipitation coarsening. However, since the thermal stability temperature of twin boundaries is only around 625 °C for the Fe-Mn-based HEAs[39], twins tend to decompose as the recrystallized grains grow, ultimately leaving behind the band-like $M_{23}C_6$ precipitates distributed within grains or across grain boundaries. These band-like precipitates that nucleate along the original deformation twin boundaries not only enhance strength but also weaken the precipitation of $M_{23}C_6$ along grain boundaries. Furthermore, the presence of precipitates significantly inhibits grain boundary migration[30,35]. In FG regions, with a high density of precipitates, grain growth is restricted, resulting in the smaller grains. In contrast, in CG regions, the nucleation rate of recrystallization and precipitates is low, which has a weak hindering effect on grain boundary migration, resulting in rapid grain growth and formation of CG regions. Interestingly, as annealing time is further extended, the high-density precipitates in the FG regions continue to pin the grain boundaries effectively, while the lower-density precipitates in the CG regions allow further grain growth, thereby increasing the grain size difference between the CG and the FG regions.

Strengthening mechanisms

The C3 alloy exhibits an excellent combination of strength and ductility, with the significantly improved yield and tensile strengths compared to the C0 and C1 alloys. Subsequently, we analyze the sources of strengthening in the C0, C1, and C3 alloys at their yielding point and an engineering strain of 42%. Since all three alloys are in the fully recrystallized state, the strength contribution from dislocations should be minor and close to each other[40], so the dislocation-induced strengthening was ignored in the calculation. Their yield strength contributions include solid solution strengthening from atoms other than carbon (σ_0), interstitial solid solution strengthening from C atoms (σ_C), grain boundary strengthening (σ_G), and precipitation strengthening (σ_P).

For the C0 alloy, the strength comprises only σ_0 and σ_G. According to the classical Hall-Petch formula[29], yield strength of the alloy can be expressed as:

$$\sigma_Y = \sigma_0 + k \times \frac{1}{\sqrt{d}} \tag{1}$$

where σ_G is the yield strength, d is the average diameter of the recrystallized grains, and k is the Hall-Petch coefficient. By fitting the relationship between grain size and yield strength for the C0 alloy with various grain sizes (as shown in Supplementary Figure 6, with tensile properties and Hall-Petch coefficient fitting illustrated in Supplementary Figure 7), σ_0 and k_{C1} were determined to be 134 MPa and 416 MPa/μm$^{1/2}$, respectively.

Similarly, the Hall-Petch coefficient for the C1 alloy was determined as 423 MPa/μm$^{1/2}$. Due to the presence of precipitates in the C3 alloy, it is difficult to determine its Hall-Petch coefficient directly. The Hall-Petch coefficients for the C0 and C1 alloys are similar, thus we assume that the coefficient for the C3 alloy is ~420 MPa/μm$^{1/2}$, which is taken to be an average value of C0 and C1 alloys.

For the C0 alloy, with an average grain size of 19.9 μm, its grain boundary strengthening is 93 MPa. For the C1 alloy, with an average grain size of 18.8 μm, the grain boundary strengthening is 98 MPa. The C3 alloy can be subdivided into a CG region which occupies 56.6% of the area and has an average grain size of 21.6 μm, and a FG region which occupies 43.4% of the area and has an average grain size of 5.9 μm. Thus, its strength contribution can be evaluated using the rule of mixtures:

$$\sigma_G = f_C \times k \times \frac{1}{\sqrt{d_C}} + f_F \times k \times \frac{1}{\sqrt{d_F}} \tag{2}$$

here, f_{CG} and f_{FG} are the area fractions of the CG and FG regions, and d_{CG} and d_{FG} are the average grain sizes of the regions, respectively. The grain boundary-induced strengthening for the C3 alloy was then determined as 126 MPa.

Next, we calculated σ_C for the C1 alloy through interpolation. Yield strength of the C1 alloy is composed of σ_0, σ_C, and σ_G, resulting in σ_0 = 33 MPa for the C1 alloy. To estimate the strength contribution from 1 at.% C, σ_C for the C0.5 alloy was also calculated as 8 MPa using the same method. Specifically, the grain boundary strengthening of the C0.5 alloy, with an average grain size of 18.4 μm [Supplementary Figure 8], is 98 MPa. By performing linear fitting on σ_C for the C0, C0.5, and C1 alloys [Supplementary Figure 9], we determined that each 1 at.% C contributed ~33 MPa of solid solution strengthening. The measured C content of the C3 alloy was 2.29 at.% [Supplementary Table 2], leading to an estimated σ_C of 76 MPa.

Finally, the C3 alloy contains a significant amount of $M_{23}C_6$ precipitates. Due to the minimum size of the precipitates being tens of nanometers, dislocations primarily move by bypassing these precipitates through the Orowan mechanism (as illustrated in Figure 10G and H). The strengthening contribution of precipitation can be calculated using[41,42]:

$$\sigma_P = \frac{0.13Gb}{\lambda}\ln(\frac{r}{b}) \tag{3}$$

where λ is the interparticle spacing, r is the radius of the precipitate, and b is the magnitude of the Burgers vector ($b = \sqrt{2}a/2$). The value of λ can be approximately evaluated as follows[41,43]:

$$\lambda \approx d_P \times \left[\left(\frac{1}{2V_P}\right)^{\frac{1}{3}} \text{-}1\right] \tag{4}$$

here, d_P represents the diameter of precipitates, and V_P denotes the volume fraction of precipitates. As previously mentioned, the average diameter of the small precipitates within grains is 73.1 nm. The precipitate fraction in the CG region is 3.4%, while in the FG region, the volume fraction of precipitates is 10.7%. The average diameter of the larger intergranular precipitates is 182.4 nm, with a volume fraction of 1.5%. Therefore, the strength contributions from precipitates in the CG region, FG region, and intergranular areas are 56 MPa, 90 MPa, and 23 MPa, respectively. The total σ_P of the alloy is 169 MPa. Consequently, the calculated total yield strength of the C3 alloy is 505 MPa, which is consistent with the measured yield strength of 500 MPa.

At an engineering strain of 42%, the flow stress originates from σ_0, σ_C, σ_G, σ_P, dislocation strengthening (σ_D), and deformation twinning-induced strengthening (σ_T). Firstly, after tensile deformation, high-density dislocations are generated in the alloy, which plays an important role in increasing the flow stress. The dislocation density (σ_P) is calculated using[14,29]:

$$\rho = \frac{2\theta}{\mu b} \tag{5}$$

where θ is the misorientation angle, evaluated by the average KAM value obtained from EBSD, and μ is the step size of EBSD mapping (0.08 μm). The calculated dislocation densities for the C0, C1, and C3 alloys are 2.80×10^{15}, 2.54×10^{15} and 5.28×10^{15} m^{-2}, respectively. The strengthening contributions due to dislocations (σ_D) for the three alloys are calculated according to[44]:

$$\sigma_D = M\alpha Gb\sqrt{\rho} \tag{6}$$

where M is the Taylor factor (3.06) and α is a constant (0.2)[45]. Therefore, the contributions from dislocations in the C0, C1, and C3 alloys are 364 MPa, 347 MPa, and 500 MPa, respectively.

Additionally, deformation twining occurs in the alloys during tensile deformation [Figure 10]. The continuous activation of these twinning significantly refines the microstructure, thereby enhancing the flow stress of the material. By subtracting σ_0, σ_C, σ_G, σ_P and σ_D from the measured yield strength, the σ_T values for the three alloys are calculated to be 137 MPa, 258 MPa, and 382 MPa, respectively. The results indicate that the contribution of twin boundaries to strength of the C3 alloy is the largest, which may be attributed to the limited carbon content of only 2.29 at.% in the alloy matrix. This means that the practical increase in SFE induced by interstitial carbon is not high enough to substantially change the deformation mode. Additionally, grain size is another important factor affecting the activation of mechanical twins[16,46]. The presence of coarse grains in the C3 alloy tends to promote extensive twining, leading to the more significant strengthening induced by the twin boundaries. The strength contribution for each alloy is illustrated in Figure 13. Compared to the C0 alloy, the yield strength increment of C3 alloy mainly comes from precipitation strengthening (145 MPa) and interstitial solid solution induced strengthening (76 MPa). This explains why both CG and FG regions of the C3 alloy exhibit significantly higher microhardness than the C0 alloy. After tensile deformation, the primary source of flow stress in the alloys is dislocation strengthening, which is attributed to the complex interactions between precipitates and dislocations [Figure 10G and H]. Additionally, the dynamic Hall-Petch effect induced by deformation twinning also contributes to the high flow stress in the C3 alloy. It is important to note that the total strength discussed above is considered as the sum of contributions from individual strengthening mechanisms[4,47]. However, in the context of multiphase alloys, this assumption may not be entirely accurate, as the matrix of these alloys is essentially in a state of "overall solute", lacking clear solute boundaries, and the various strengthening mechanisms are not completely independent of one another[48,49].

HDI strengthening and plastic deformation mechanisms

The C3 alloy demonstrates an excellent strength-plasticity combination, which can be attributed to its unique dual heterostructure. In this case, the CG region acts as the soft domain, while the FG region is the hard domain. The uneven distribution of precipitates in the CG and FG regions further enhances the differences in mechanical properties between the different regions. Specifically, the Vickers hardness of the CG region in the C3 alloy is measured to be 2.5 GPa, while that of the FG region can reach 3.4 GPa. Similarly, the micron-sized recrystallized grains are viewed as the soft domain, whereas the nanosized $M_{23}C_6$ precipitates are regarded as the hard domain. At the onset of deformation, both soft and hard regions undergo elastic deformation simultaneously. As deformation proceeds, the soft region begins to undergo plastic deformation, while the hard region remains in the elastic state. To facilitate the coordinated deformation between the different regions, GNDs are generated at the interface between the soft and hard regions. Results from EBSD analysis indicate that under the same strain, the dual heterostructure of the C3 alloy exhibits approximately double the dislocation density compared to the equiaxed C0 and C1 alloys. Specifically, the dislocation densities for C0, C1, and C3 alloys are 2.80×10^{15}, 2.54×10^{15}, and 5.28×10^{15} m^{-2}, respectively [Figure 9D-F].

To evaluate the HDI strengthening and hardening resulting from the heterostructure, we conducted LUR cyclic tensile experiments on the C0, C1, and C3 alloys. The engineering stress-strain and true stress-strain curves for each alloy are presented in Figure 14A and B, with an enlarged view of the individual hysteresis loops depicted in Figure 14C. The HDI stress is calculated as the average of the unloading stress (σ_u) and the reloading stress (σ_r)[50,51], as follows:

$$\sigma_{\mathrm{HDI}} = (\sigma_{\mathrm{r}} + \sigma_{\mathrm{u}})/2 \tag{7}$$

As shown in Figure 14D, both C0 and C1 alloys exhibit relatively small hysteresis loops at all stages of deformation, indicating low HDI stress for both, with a similar rate of stress increase with straining. In contrast, the C3 alloy displays larger hysteresis loops, demonstrating significantly higher HDI stress than C0 and C1 alloys at all strains, with the highest ratio of HDI stress to true strain. This indicates that the C3

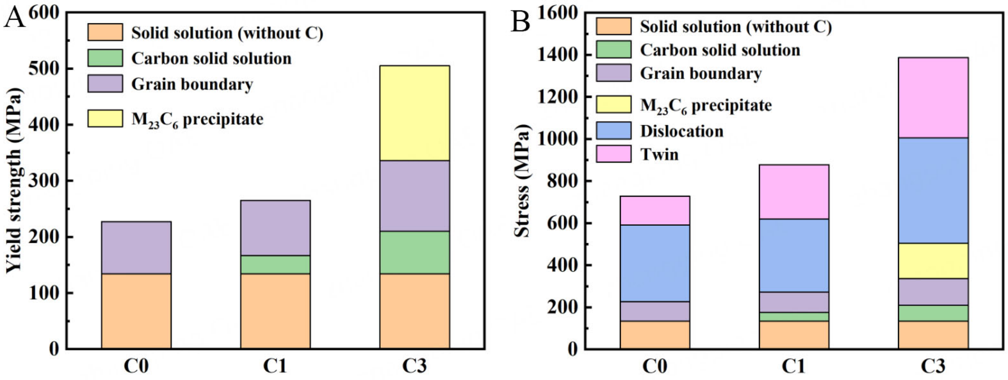

Figure 13. Strength contributions in the C0, C1 and C3 alloys at: (A) the yielding point and (B) 42% tensile strain.

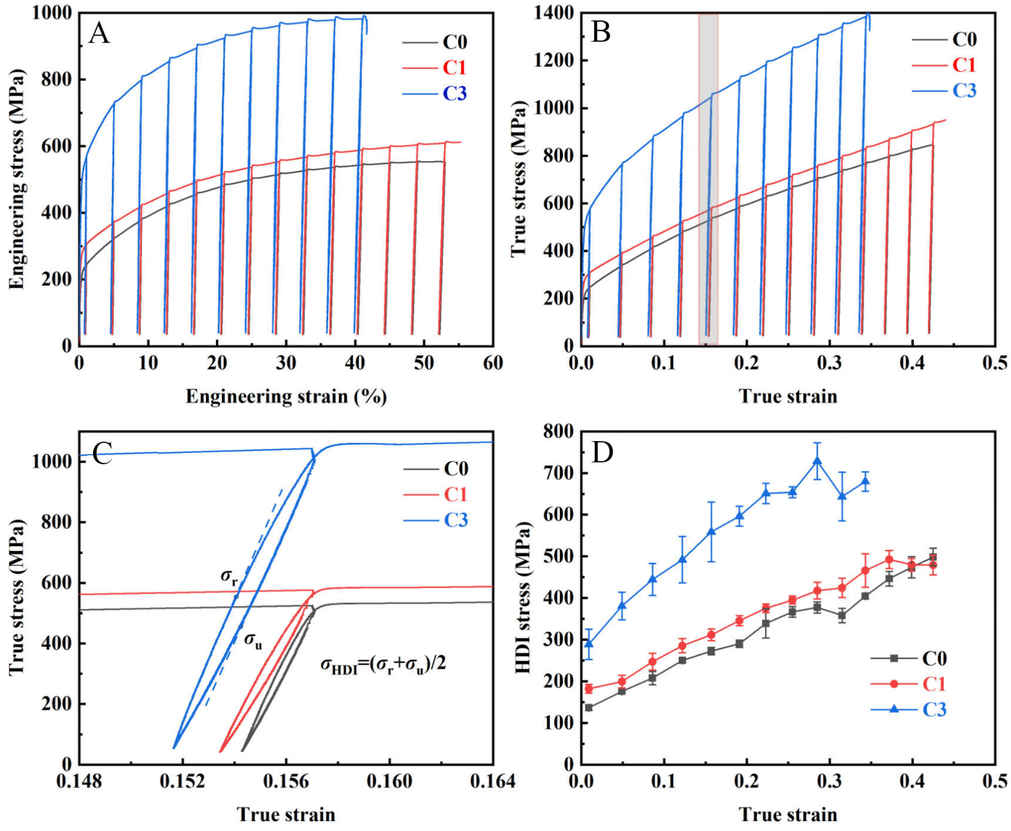

Figure 14. (A) Engineering stress-strain curves of the C0, C1 and C3 alloys obtained by LUR tests; (B) the corresponding true stress-strain curves; (C) an enlarged view of typical hysteresis loops in the shadow area in (B); (D) HDI stress as a function of true stress. LUR: Loading-unloading-reloading; HDI: hetero-deformation-induced.

alloy, due to its dual heterogeneous structure, has a greater HDI strengthening and hardening effect compared to the C0 and C1 alloys with uniform microstructures.

Furthermore, the C3 alloy exhibits optimal strain hardening ability while the strength is elevated, which can be ascribed to the following. Firstly, similar to the C0 and C1 alloys, the C3 alloy still shows significant twinning activation during tensile deformation [Figure 10]. The continuous activation of twinning refines the microstructure, thus providing the capacity for sustained plastic deformation and good work hardening[52]. The activation of twinning is closely related to the SFE, which for the solid solution-treated C3 alloy is 37.2 mJ/m^2 [Supplementary Note and Supplementary Figure 10]. For the cold-rolled and short-time annealed alloy, the SFE should be lower than this value due to a certain amount of C element precipitating from the matrix as precipitates, thereby promoting the activation of twins[53,54]. Secondly, the multiscale $M_{23}C_6$ precipitates which are unevenly distributed both within grains and between the neighboring grains also hinder dislocation motion, thereby increasing the work hardening rate of the alloy[55,56]. Finally, the difference in mechanical properties between the coarse and fine grains in the C3 alloy is a significant source of the HDI stress, and the higher density of precipitates within the FG regions increases the strength difference between coarse and fine grains. Additionally, another heterostructure forms between the precipitates and the matrix. This dual-heterostructure ultimately leads to pronounced HDI strengthening and hardening in the C3 alloy.

CONCLUSIONS

In this study, we doped FeMnCoCrCu HEA with carbon and obtained alloys with different microstructural characteristics through combined processing of cold rolling and the subsequent annealing. Notably, the C3 alloy, characterized by a dual-heterostructure, exhibits high strength and excellent plasticity combination, along with superior work hardening ability. The main conclusions are as follows:

(1) The C0 and C1 alloys possess uniform microstructures with average grain sizes of 19.9 μm and 18.8 μm, respectively. In contrast, the C3 alloy exhibits dual-heterostructure, including bimodal grain sizes, small-sized $M_{23}C_6$ precipitates within grains, and large-sized $M_{23}C_6$ precipitates at grain boundaries. Specifically, the average grain sizes in the CG and FG regions of the C3 alloy are 21.6 μm and 5.9 μm, respectively, with volume fractions of 43.4% and 56.6%. The small-sized precipitates within the grains have an average size of 73.1 nm, with volume fractions of 3.4% and 10.7% in the CG and FG regions, respectively. The large-sized intergranular precipitates have an average size of 182.4 nm and a total volume fraction of 1.5%.

(2) The C0 alloy has a yield strength of 223 MPa, tensile strength of 535 MPa, and uniform elongation of 57.1%. In contrast, the C3 alloy exhibits significantly enhanced strength and work hardening rate, with only a modest reduction in plasticity. Specifically, the C3 alloy has a yield strength of 500 MPa, tensile strength of 979 MPa, and uniform elongation of 42%.

(3) Compared to the carbon-free alloy, the enhanced yield strength of the C3 alloy primarily arises from interstitial solid solution strengthening and precipitation-induced strengthening. During the work hardening stage, the increase in flow stress in the C3 alloy mainly comes from strengthening caused by dislocations and deformation twinning.

(4) The dual-heterostructure of the C3 alloy results in significant HDI strengthening and hardening. The high HDI stress significantly enhances both yield strength and strain hardening capacity of the alloy.

DECLARATIONS

Acknowledgments

We extend our special thanks to Mr. Yujie Liu from the School of Materials Science and Engineering, Northeastern University, for his assistance with TEM characterization.

Authors' contributions

Conceived the idea and supervised the project: Jia, N.; Zhu, M.
Responsible for material preparation and experimental testing: Yuan, Y.; Wang, J.
Collaborated on data analysis and result discussions: Yuan, Y.; Min, J.; Pan, H.; Yang, Y.; Chen, W.; Jia, N.
Wrote the manuscript: Yuan, Y.; Jia, N.
All authors participated in reviewing and contributed to the final version of the manuscript.

Availability of data and materials

The data that support the findings of this study are available from the corresponding author upon reasonable request.

Financial support and sponsorship

This work was supported by the National Key Research and Development Program of China (2021YFA1200203) and the National Natural Science Foundation of China (Nos. 52371097, 51922026).

Conflicts of interest

All authors declared that there are no conflicts of interest.

Ethical approval and consent to participate

Not applicable.

Consent for publication

Not applicable.

Copyright

REFERENCES

1. Yeh, J.; Chen, S.; Lin, S.; et al. Nanostructured high-entropy alloys with multiple principal elements: novel alloy design concepts and outcomes. *Adv. Eng. Mater.* **2004**, *6*, 299-303. DOI
2. Cantor, B.; Chang, I.; Knight, P.; Vincent, A. Microstructural development in equiatomic multicomponent alloys. *Mater. Sci. Eng. A.* **2004**, *375-377*, 213-8. DOI
3. He, Z.; Jia, N.; Yan, H.; et al. Multi-heterostructure and mechanical properties of N-doped FeMnCoCr high entropy alloy. *Int. J. Plast.* **2021**, *139*, 102965. DOI
4. He, Z.; Guo, Y.; Sun, L.; et al. Interstitial-driven local chemical order enables ultrastrong face-centered cubic multicomponent alloys. *Acta. Mater.* **2023**, *243*, 118495. DOI
5. Li, Z.; Pradeep, K. G.; Deng, Y.; Raabe, D.; Tasan, C. C. Metastable high-entropy dual-phase alloys overcome the strength-ductility trade-off. *Nature* **2016**, *534*, 227-30. DOI PubMed
6. Marques, F.; Balcerzak, M.; Winkelmann, F.; Zepon, G.; Felderhoff, M. Review and outlook on high-entropy alloys for hydrogen storage. *Energy. Environ. Sci.* **2021**, *14*, 5191-227. DOI
7. Liu, Y.; Du, H.; Zhang, X.; Yang, Y.; Gao, M.; Pan, H. Superior catalytic activity derived from a two-dimensional Ti_3C_2 precursor towards the hydrogen storage reaction of magnesium hydride. *Chem. Commun.* **2016**, *52*, 705-8. DOI
8. Pang, Y.; Liu, Y.; Gao, M.; et al. A mechanical-force-driven physical vapour deposition approach to fabricating complex hydride nanostructures. *Nat. Commun.* **2014**, *5*, 3519. DOI
9. Zhang, X.; Liu, Y.; Ren, Z.; et al. Realizing 6.7 wt% reversible storage of hydrogen at ambient temperature with non-confined ultrafine magnesium hydrides. *Energy. Environ. Sci.* **2021**, *14*, 2302-13. DOI
10. Min, J.; Yuan, Y.; He, Z.; Zhu, M.; Chen, W.; Jia, N. Superior mechanical properties and multiple strengthening mechanisms of a V-alloyed FeMnCoCr high-entropy alloy. *Mater. Sci. Eng. A.* **2024**, *902*, 146614. DOI
11. Li, Z.; Raabe, D. Strong and ductile non-equiatomic high-entropy alloys: design, processing, microstructure, and mechanical properties. *JOM.* **2017**, *69*, 2099-106. DOI PubMed PMC
12. Li, Z.; Tasan, C. C.; Springer, H.; Gault, B.; Raabe, D. Interstitial atoms enable joint twinning and transformation induced plasticity in strong and ductile high-entropy alloys. *Sci. Rep.* **2017**, *7*, 40704. DOI PubMed PMC
13. Zhang, H.; Zhao, M.; Zhang, J.; Zhao, X.; Fang, F.; Jia, N. Ultrahigh strength induced by multiple heterostructures in a FeMnCoCrN

high-entropy alloy fabricated by powder metallurgy technique. *Mater. Sci. Eng. A.* **2022**, *846*, 143304. DOI

14. Su, J.; Raabe, D.; Li, Z. Hierarchical microstructure design to tune the mechanical behavior of an interstitial TRIP-TWIP high-entropy alloy. *Acta. Mater.* **2019**, *163*, 40-54. DOI
15. Yuan, Y.; Wang, J.; Wei, J.; Chen, W.; Yan, H.; Jia, N. Cu alloying enables superior strength-ductility combination and high corrosion resistance of FeMnCoCr high entropy alloy. *J. Alloy. Compd.* **2024**, *970*, 172543. DOI
16. Li, Z.; Tasan, C. C.; Pradeep, K. G.; Raabe, D. A TRIP-assisted dual-phase high-entropy alloy: grain size and phase fraction effects on deformation behavior. *Acta. Mater.* **2017**, *131*, 323-35. DOI
17. Zhu, Y.; Wu, X. Heterostructured materials. *Prog. Mater. Sci.* **2023**, *131*, 101019. DOI
18. Zhu, Y. T.; Wu, X. L. Introduction to heterostructured materials. Oxford: Elsevier; 2023. pp. 9-10. Available from: https://doi.org/10.1016/C2021-0-00963-9. [Last accessed on 17 Mar 2025].
19. Li, A.; Yu, P.; Gao, Y.; Dove, M.; Li, G. Ultra-high strength and excellent ductility high entropy alloy induced by nano-lamellar precipitates and ultrafine grain structure. *Mater. Sci. Eng. A.* **2023**, *862*, 144286. DOI
20. Yang, Y.; Liu, Y.; Jiang, S.; et al. Achieving exceptional strength and ductility combination in a heterostructured Mg-Y alloy with densely refined twins. *J. Mater. Scie. Technol.* **2024**, *189*, 132-45. DOI
21. Wu, X.; Yang, M.; Yuan, F.; et al. Heterogeneous lamella structure unites ultrafine-grain strength with coarse-grain ductility. *Proc. Natl. Acad. Sci. U. S. A.* **2015**, *112*, 14501-5. DOI PubMed PMC
22. Li, J.; Cao, Y.; Gao, B.; Li, Y.; Zhu, Y. Superior strength and ductility of 316L stainless steel with heterogeneous lamella structure. *J. Mater. Sci.* **2018**, *53*, 10442-56. DOI
23. Zhang, Z.; Orlov, D.; Vajpai, S. K.; Tong, B.; Ameyama, K. Importance of bimodal structure topology in the control of mechanical properties of a stainless steel. *Adv. Eng. Mater.* **2015**, *17*, 791-5. DOI
24. Zhang, Z.; Vajpai, S. K.; Orlov, D.; Ameyama, K. Improvement of mechanical properties in SUS304L steel through the control of bimodal microstructure characteristics. *Mater. Sci. Eng. A.* **2014**, *598*, 106-13. DOI
25. Yang, Y.; Liu, Y.; Yan, S.; et al. On the micromechanism of superior strength and ductility synergy in a heterostructured Mg-2.77Y alloy. *J. Magnes. Alloys.* **2024**, *12*, 2793-811. DOI
26. Pu, Z.; Cai, S.; Dai, L. Effective strengthening and toughening in high entropy-alloy by combining extrusion machining and heat treatment. *Scr. Mater.* **2022**, *213*, 114630. DOI
27. Sun, W.; Luo, J.; Chan, Y. Y.; Luan, J.; Yang, X. An extraordinary-performance gradient nanostructured Hadfield manganese steel containing multi-phase nanocrystalline-amorphous core-shell surface layer by laser surface processing. *J. Mater. Sci. Technol.* **2023**, *134*, 209-22. DOI
28. Sun, Y.; Kong, X.; Wang, Z. Superior mechanical properties and deformation mechanisms of a 304 stainless steel plate with gradient nanostructure. *Int. J. Plast.* **2022**, *155*, 103336. DOI
29. Wang, Z.; Lu, W.; Zhao, H.; et al. Ultrastrong lightweight compositionally complex steels via dual-nanoprecipitation. *Sci. Adv.* **2020**, 6. DOI PubMed PMC
30. Li, G.; Liu, M.; Lyu, S.; et al. Simultaneously enhanced strength and strain hardening capacity in FeMnCoCr high-entropy alloy via harmonic structure design. *Scr. Mater.* **2021**, *191*, 196-201. DOI
31. Jiang, S.; Peng, R. L.; Hegedűs, Z.; et al. Micromechanical behavior of multilayered Ti/Nb composites processed by accumulative roll bonding: an in-situ synchrotron X-ray diffraction investigation. *Acta. Mater.* **2021**, *205*, 116546. DOI
32. Li, A.; Liu, X.; Li, R.; et al. Double heterogeneous structures induced excellent strength-ductility synergy in $Ni_{40}Co_{30}Cr_{20}A_{15}Ti_5$ medium-entropy alloy. *J. Mater. Scie. Technol.* **2024**, *181*, 176-88. DOI
33. Guo, S.; Ma, Z.; Xia, G.; et al. Pursuing ultrastrong and ductile medium entropy alloys via architecting nanoprecipitates-enhanced hierarchical heterostructure. *Acta. Mater.* **2024**, *263*, 119492. DOI
34. Zhao, G.; Zhang, J.; Li, J.; Li, H.; Liu, H.; Ma, L. Effect of copper on edge cracking behavior and microstructure of rolled austenitic stainless steel plate. *J. Iron. Steel. Res. Int.* **2022**, *29*, 281-94. DOI
35. Gao, J.; Jiang, S.; Zhang, H.; et al. Facile route to bulk ultrafine-grain steels for high strength and ductility. *Nature* **2021**, *590*, 262-7. DOI PubMed PMC
36. Wang, X.; Xu, L.; Jiao, L.; et al. Inhibition of the intergranular brittleness of HR3C heat-resistant steel by strain-aging induced nano-$M_{23}C_6$ dispersion precipitation. *J. Mater. Scie. Technol.* **2025**, *213*, 288-99. DOI
37. Weygand, D.; Bréchet, Y.; Lépinoux, J. Zener pinning and grain growth: a two-dimensional vertex computer simulation. *Acta. Mater.* **1999**, *47*, 961-70. DOI
38. Humphreys, F.; Ardakani, M. Grain boundary migration and zener pinning in particle-containing copper crystals. *Acta. Mater.* **1996**, *44*, 2717-27. DOI
39. Moon, J.; Bouaziz, O.; Kim, H. S.; Estrin, Y. Twinning Engineering of a CoCrFeMnNi high-entropy alloy. *Scr. Mater.* **2021**, *197*, 113808. DOI
40. He, Z.; Jia, N.; Wang, H.; Yan, H.; Shen, Y. Synergy effect of multi-strengthening mechanisms in FeMnCoCrN HEA at cryogenic temperature. *J. Mater. Sci. Technol.* **2021**, *86*, 158-70. DOI
41. Zhang, Z.; Chen, D. Consideration of Orowan strengthening effect in particulate-reinforced metal matrix nanocomposites: a model for predicting their yield strength. *Scr. Mater.* **2006**, *54*, 1321-6. DOI
42. Wu, Y.; Zhao, X.; Chen, Q.; et al. Strengthening and fracture mechanisms of a precipitation hardening high-entropy alloy fabricated by selective laser melting. *Virtual. Phys. Prototyp.* **2022**, *17*, 451-67. DOI

43. Zhang, Q.; Chen, D. A model for predicting the particle size dependence of the low cycle fatigue life in discontinuously reinforced MMCs. *Scr. Mater.* **2004**, *51*, 863-7. DOI
44. Mecking, H.; Kocks, U. Kinetics of flow and strain-hardening. *Acta. Metall.* **1981**, *29*, 1865-75. DOI
45. Dini, G.; Ueji, R.; Najafizadeh, A.; Monir-vaghefi, S. Flow stress analysis of TWIP steel via the XRD measurement of dislocation density. *Mater. Sci. Eng. A.* **2010**, *527*, 2759-63. DOI
46. Liu, S.; Xiong, Z.; Guo, H.; Shang, C.; Misra, R. The significance of multi-step partitioning: Processing-structure-property relationship in governing high strength-high ductility combination in medium-manganese steels. *Acta. Mater.* **2017**, *124*, 159-72. DOI
47. Sun, L. F.; He, Z. F.; Jia, N.; et al. Local chemical order enables an ultrastrong and ductile high-entropy alloy in a cryogenic environment. *Sci. Adv.* **2024**, *10*, eadq6398. DOI PubMed PMC
48. Basu, I.; De, H. J. T. Strengthening mechanisms in high entropy alloys: Fundamental issues. *Scr. Mater.* **2020**, *187*, 148-56. DOI
49. Biswas, K.; Yeh, J.; Bhattacharjee, P. P.; Dehosson, J. T. High entropy alloys: key issues under passionate debate. *Scr. Mater.* **2020**, *188*, 54-8. DOI
50. Zhu, Y.; Wu, X. Perspective on hetero-deformation induced (HDI) hardening and back stress. *Mater. Res. Lett.* **2019**, *7*, 393-8. DOI
51. Yang, M.; Pan, Y.; Yuan, F.; Zhu, Y.; Wu, X. Back stress strengthening and strain hardening in gradient structure. *Mater. Res. Lett.* **2016**, *4*, 145-51. DOI
52. Picak, S.; Liu, J.; Hayrettin, C.; et al. Anomalous work hardening behavior of $Fe_{40}Mn_{40}Cr_{10}Co_{10}$ high entropy alloy single crystals deformed by twinning and slip. *Acta. Mater.* **2019**, *181*, 555-69. DOI
53. Ming, K.; Bi, X.; Wang, J. Strength and ductility of CrFeCoNiMo alloy with hierarchical microstructures. *Int. J. Plast.* **2019**, *113*, 255-68. DOI
54. Laplanche, G.; Kostka, A.; Horst, O.; Eggeler, G.; George, E. Microstructure evolution and critical stress for twinning in the CrMnFeCoNi high-entropy alloy. *Acta. Mater.* **2016**, *118*, 152-63. DOI
55. Wang, J.; Zou, J.; Yang, H.; et al. Ultrastrong and ductile $(CoCrNi)_{94}Ti_3Al_3$ medium-entropy alloys via introducing multi-scale heterogeneous structures. *J. Mater. Sci. Technol.* **2023**, *135*, 241-9. DOI
56. Liu, X.; Li, R.; Fan, X.; et al. Excellent strength-ductility combination in $Co_{36}Cr_{15}Fe_{18}Ni_{18}Al_8Ti_4Mo_1$ multi-principal element alloys by dual-morphology B2 precipitates strengthening. *J. Mater. Sci. Technol.* **2023**, *134*, 60-6. DOI